Environ. Sci. Technol. **2003**, *37,* 2363−2370

Microscopic Observations of Reductive Manganite Dissolution under Oxic Conditions

YOUNG-SHIN JUN AND SCOT T. MARTIN*
Division of Engineering and Applied Sciences,
Harvard University, Cambridge, Massachusetts 02138

At oxic/anoxic transition zones, manganese release from (hydr)oxide minerals into aqueous solution is a dynamic balance between mineral dissolution and Mn^{2+}(aq) oxidation and precipitation, which are processes respectively promoted by organic reductants and molecular oxygen. We employ a flow-through atomic force microscope reactor (AFM-R) to investigate the reductive dissolution of the {010} surface of manganite (γ-MnOOH) across a range of pH values and ascorbic acid concentrations in aqueous solutions equilibrated with atmospheric CO_2 and O_2. The apparent dissolution rate increases with higher ascorbic acid concentrations and lower pH values. Concurrent changes in surface morphology show that dissolution proceeds at low pH via etching and step retreat, while at high pH dissolution is concurrent with precipitation. The precipitates are characterized ex situ by X-ray photoelectron spectroscopy (XPS) and found to be Mn^{III}-oxide. The onset of precipitation is consistent with an analysis of the thermodynamic driving forces for the reactions of a two-step mechanism. In the first step, Mn^{2+} is released to aqueous solution by reduction of γ-MnOOH in reaction with ascorbic acid. This step is thermodynamically favorable under all conditions employed. In the second step, which leads to precipitation, surface adsorbed Mn^{2+} is oxidized by O_2 to yield a Mn^{III}-oxide precipitate. This step is thermodynamically possible only at pH > 5 for our experimental conditions. When the second step is active, the apparent dissolution rate equals the intrinsic dissolution rate minus the precipitation rate. Analysis of the growth rates observed in AFM indicates the precipitation rate reaches 71% of the intrinsic dissolution rate under some reactor conditions. Comparison of our γ-MnOOH results to literature reports for Mn^{2+} oxidation on γ-FeOOH indicates γ-MnOOH is a more effective surface catalyst by a factor of 10^8.

Introduction

Manganese oxide minerals have important roles in the chemical cycles and biological activities at and near the earth's surface. As a consequence of mineral dissolution and precipitation, Mn-bearing minerals strongly affect groundwater chemistry, including perturbation and in some cases control of pH and pE (*1*, *2*). Bioavailable manganese is also a key micronutrient for all life forms (*3*−*5*) due to its role as a principal cofactor in many enzymes (*6*−*9*). Although Mn^{2+}(aq) is thermodynamically favored at low pH values and under anoxic conditions (Figure 1), to become bioavailable aqueous Mn^{2+} must be dissolved from Mn^{III} and Mn^{IV} oxide matrices. This reaction is slow in pure water. An important relatively rapid pathway is the reductive dissolution of manganese (hydr)oxide minerals by aqueous organic molecules (*10*−*12*). The organic reductants are exuded by roots and microorganisms in the rhizosphere (*13*−*15*), and there is an extensive suite of redox couples between organic molecules and manganese species.

Within the complex array of redox couples, one governing inorganic master variable is the activity of molecular oxygen, as quantified in pE. The pE-pH diagram in Figure 1 shows that an important sink for aqueous Mn^{2+} is the oxic/anoxic transitions occurring in the soil horizon, in the rhizosphere, and in biofilms (*9*, *16*, *17*). Mn^{2+} is catalytically oxidized by O_2 at particulate surfaces to form coatings of Mn^{III} and Mn^{IV} oxides on mineral soil particulate substrates (*6*, *18*). At oxic/anoxic interfaces, simultaneous with precipitation of Mn^{III} and Mn^{IV} coatings, organic molecules concurrently continue to promote the dissolution of the Mn^{III} and Mn^{IV} oxides. The morphology and extent of surface coatings are a dynamic balance between these oxidation and reduction processes. Hem discusses the transformations and aging of Mn oxide minerals and emphasized the important role of diffusion of O_2 to the mineral surfaces and oxidation of surface-adsorbed Mn^{2+} there (*19*).

The need to understand the complex nature of the dynamic balance between dissolution and precipitation motivates the work reported in this paper on detailed studies of reductive dissolution under oxic conditions. Several previous studies have addressed the kinetic aspects of the reductive dissolution of manganese oxides by monitoring the production rate of Mn^{2+}(aq), both in particulate suspensions (*3*, *10*, *11*, *20*−*23*) and from films of manganese oxides (*24*, *25*). Through inference, these macroscopic studies offer hypotheses on the microscopic surface processes consistent with the observed overall dissolution rates. Structure−activity relationships for organic reductants and dissolution rates under anoxic conditions have been extensively investigated (*10*, *11*, *20*). Other studies have focused on both the homogeneous and heterogeneous oxidation kinetics (i.e., precipitation) of Mn^{2+} (*6*, *18*, *26*−*29*). Aqueous Mn^{2+} oxidation in oxic particulate suspensions is initially slow, when homogeneous oxidation is active, and is followed by a switch to more rapid heterogeneous oxidation (i.e., surface catalyzed oxidation) as particulate manganese oxide products build up (*6*, *18*, *26*, *27*, *30*). Junta and Hochella (*31*) studied Mn^{2+} oxidation for $7.8 < pH < 8.7$ on a variety of surfaces, including goethite, hematite, and albite, in the presence of O_2. A Mn^{III} precipitate, principally β-MnOOH followed in smaller amounts by γ-MnOOH, is observed. Despite these successes, our current understanding remains limited about the detailed morphological surface processes accompanying reductive dissolution, even more so at an organic-bearing oxic interface where dissolution and precipitation occur simultaneously. A kinetic and mechanistic understanding of processes at the microscopic level is necessary to construct robust predictive models at the macroscopic level.

In the current paper, the dissolution rate of manganite (γ-MnOOH) is investigated across a range of pH values and reductant concentrations in aqueous solutions equilibrated with atmospheric CO_2 and O_2. The reductant employed is ascorbic acid ($pK_{a1} = 4.17$ and $pK_{a2} = 11.57$) (*32*). Ascorbic acid has been widely employed for the reductive dissolution of iron oxides (*10*, *33*−*36*). Changes in surface morphology are observed by atomic force microscopy (AFM), while the aqueous manganese concentration is simultaneously quan-

---

* Corresponding author phone: (617)495-7620; fax: (617)495-9837; e-mail: scot_martin@harvard.edu.

10.1021/es026254x CCC: $25.00

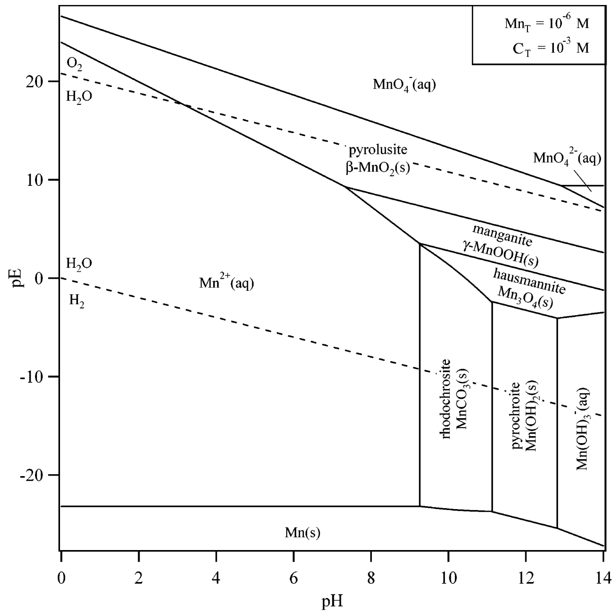

FIGURE 1. pE-pH diagram of the Mn/CO$_2$/H$_2$O system drawn for Mn$_T$ = 10^{-6} M and C_T = 10^{-3} M at 298 K. The water stability field is shown for P_{O_2} = 1 atm and P_{H_2} = 1 atm. Thermodynamic data are from Lindsay (*59*).

tified by graphite furnace-atomic absorption spectroscopy (GF-AAS) (*37*). Surface products are characterized by X-ray photoelectron spectroscopy (XPS). As reported below, the dissolution rates correlate with the qualitative surface changes observed in the AFM micrographs. The observations are rationalized by chemical mechanisms that are constrained by free energy driving forces, which depend on pH and ascorbic acid concentration.

Experimental Section

Manganite, obtained from Hawthorneden (Atikokan, Ontario), is characterized for chemical purity with proton-induced X-ray emission spectroscopy (PIXE, Cambridge Particle Accelerator Facility, Harvard University). The sample is 99.93% Mn, 0.03% Ca, 0.02% Ni, 0.01% Cu, and 0.01% As. Analysis by powder X-ray diffractometry (XRD) confirms that the sample is manganite. For the dissolution experiments described below, flat manganite surfaces, at least 2 × 2 mm^2 and 1 mm thick, are prepared by fracture of a large sample with a razor blade struck by a hammer. Each flat sample is mounted with warmed sealing wax (Cavex, Holland) on a steel puck. Only the top surface remains exposed. XRD sample analysis confirms that the surface plane is dominantly of {010} orientation.

Dissolution experiments are conducted by placing the freshly prepared sample into a flow-through reactor (*37*). A schematic diagram of the experimental apparatus, which consists of an atomic force microscope equipped with a fluid cell (Nanoscope IIIa Multimode SPM, Digital Instruments), a syringe driver (Orion Sage, Beverly, MA), and a fraction collector (Retriever 500, Isco, Lincoln, NE), is shown in Figure 2. Under the experimental protocol, dissolution liquor is pumped from 60 mL syringes at 0.6 mL min^{-1}. During an experiment several syringes are interchanged to adjust pH and the aqueous ascorbic acid concentration. The fluid cell effluent passes through a vertical flow pH electrode (Cole-Parmer) and is collected in 4.2 mL aliquots by a fraction collector. The aqueous manganese concentration is determined off-line by GF-AAS (Perkin-Elmer AAnalyst 300).

While the solution is flowing through the fluid cell, AFM images are collected in contact mode with oxide-sharpened Si$_3$N$_4$ nanoprobes (force constant of 0.12 N m^{-1}, radius of curvature of 5−40 nm, Digital Instruments). Images, ranging in size from 5 × 5 to 10 × 10 μm^2, are scanned at 2 Hz. A CCD camera equipped with a magnifying head is employed to capture optical images of the manganite sample. These images are analyzed off-line to determine geometric sample surface area.

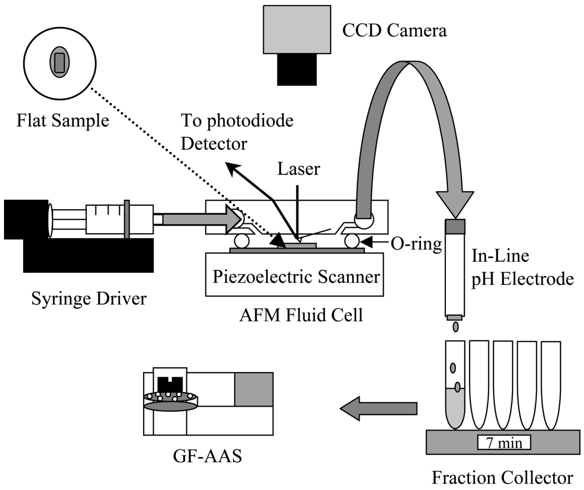

FIGURE 2. Apparatus for AFM/flow-through reactor experiments. A syringe pump drives solution via FEP tubing (low gas permeability) through the AFM fluid cell. The effluent passes through an in-line pH meter and is collected in test tubes by a fraction collector for off-line GF-AAS analysis of [Mn^{2+}].

Dissolution liquors, which are prepared for the syringes, have ascorbic acid concentrations of 10^{-5}, 10^{-4}, 10^{-3}, and 10^{-2} M and pH values of 3.2, 4.0, 5.5, 6.3, and 7.3. Using these concentrations, a matrix of 20 different dissolution experiments is carried out, along with control experiments having no ascorbic acid. The pH values are adjusted by addition of HCl (37%, EM Science) or NaOH (98.6%, J. T. Baker). Solutions are prepared from L-ascorbic acid (99.9%, Fisher Scientific). Solutions are equilibrated with atmospheric CO$_2$ and O$_2$ at 298 K. The ionic strength of each solution is adjusted to 10^{-2} M with NaNO$_3$ (100%, Mallinckrodt).

In separate experiments, several manganite samples are exposed to 0.1 M ascorbic acid at either pH = 2.4 or 5.9 for periods of 1, 3, and 24 h. X-ray photoelectron spectra are collected for these samples as well as several reference minerals, including pyrolusite, hausmannite, and untreated manganite. A Surface Science Laboratories SSX-100 X-ray photoelectron spectrometer (MRSEC, Harvard University), equipped with a monochromatized AlKα X-ray source and characterized by a base pressure of 10^{-9} Torr in the analytical chamber, is employed to record the XPS spectra. Scans for Mn, O, and C are recorded using a 600 μm spot size and a fixed pass energy of 50 eV. For data analysis, the count intensities are arbitrarily normalized to account for the varying surface areas of the irregularly shaped manganite samples employed. The binding energies are corrected according to the C 1s adventitious carbon peak being located at 284.6 eV (*38*, *39*).

Results

The manganite dissolution rate versus time is shown in Figure 3 for several aqueous solution conditions. The dissolution rate (R) is calculated from [Mn^{2+}], the manganite sample surface area (A), and the reactor flow rate (F), as follows (*40*):

$$R = \frac{([Mn^{2+}]_{\text{effluent}} - [Mn^{2+}]_{\text{influent}})F}{A} \qquad (1)$$

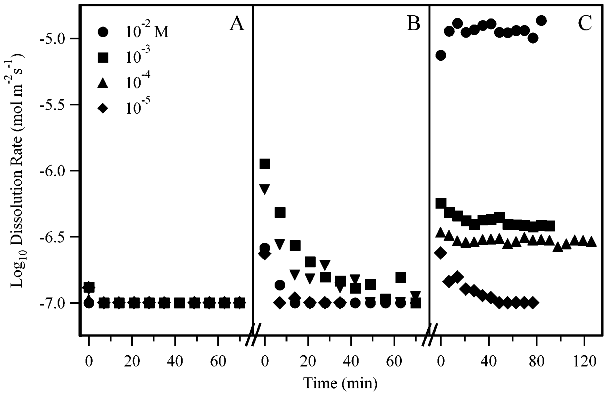

FIGURE 3. Apparent manganite dissolution rate versus time. (A) Water (pH = 5.6). (B) pH adjusted to 2.7 (HCl) in 10 mM $NaNO_3$. (C) Ascorbic acid added from 10^{-5} to 10^{-2} M as indicated in the figure legend. pH adjusted to 4.0 with HCl or NaOH, as necessary, in 10 mM $NaNO_3$. Conditions: 0.6 mL min^{-1} flow, 298 K. Flow solutions equilibrated with atmospheric O_2 and CO_2. Dissolution rates of 10^{-7} mol m^{-2} s^{-1} should be understood as upper limits.

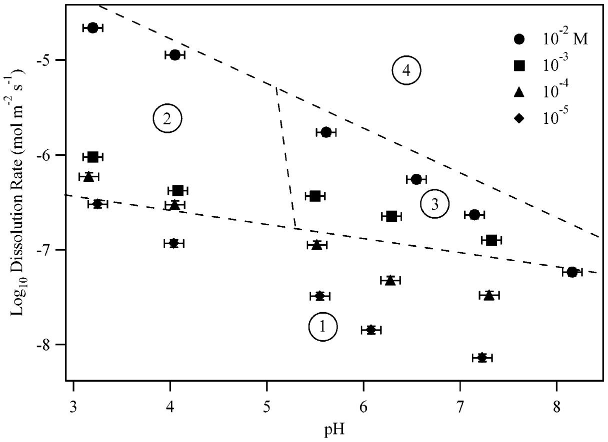

FIGURE 4. Summary of apparent steady-state manganite dissolution rates versus pH for several ascorbic acid concentrations. See further reactor conditions in caption to Figure 3. Four subdivided regions are shown in Figure 4, as follows: (1) No surface changes apparent in concurrent AFM imaging. (2) Etching and step retreat apparent in imaging. (3) Precipitates apparent in imaging when O_2 is present. (4) No experiments conducted in this region.

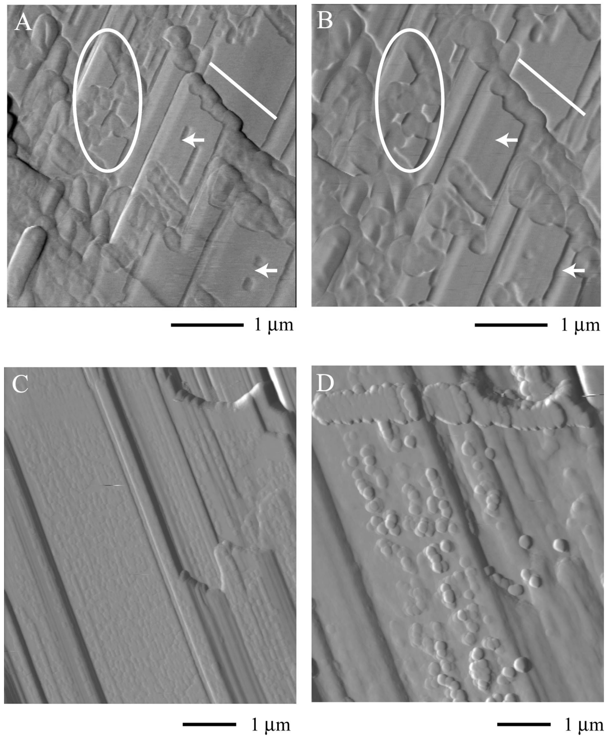

FIGURE 5. AFM deflection-mode micrographs of surfaces changes observed in situ at 298 K during exposure of manganite to ascorbic acid at acidic and neutral pH values. Images {*A*, *B*} and {*C*, *D*}, respectively, show surface changes characteristic of regions 2 and 3 in Figure 4. (A) pH = 3.2, 10 mM $NaNO_3$. (B) Same as (A) after exposure to 1 mM ascorbic acid for 95 min. (C) pH = 7.2, 10 mM $NaNO_3$. (D) Same as (C) after exposure to 10 mM ascorbic acid for 65 min. In height images (not shown), *z*-scale is 125 nm for {*A*, *B*} and 400 nm for {*C*, *D*}.

Analysis shows $[Mn^{2+}]_{influent}$ is below the detection limit. The minimum instantaneous dissolution rate accurately quantified by this apparatus is 10^{-7} mol m^{-2} s^{-1}, while the time-averaged dissolution rate (60 min) allows quantification to as low as 10^{-8} mol m^{-2} s^{-1}. As shown in Figure 3, in the absence of ascorbic acid the dissolution rate at pH = 5.6 is less than 10^{-7} mol m^{-2} s^{-1}. Upon changing syringes to pH = 2.7, there is an initial transient increase in dissolution rate (*41*, *42*) followed by relaxation toward 10^{-7} mol m^{-2} s^{-1}. Addition of ascorbic acid at pH = 4.0 yields an increase in the steady-state dissolution rate by up to 2 orders of magnitude for the highest ascorbic acid concentration employed (10^{-2} M), and the increase in dissolution rate is monotonic with the increase in ascorbic acid concentration. For the lowest ascorbic concentration studied (viz. 10^{-5} M), there is no detectable difference between this dissolution liquor and the control liquor containing no ascorbic acid. The results for pH values other than 4.0 are qualitatively similar to those shown in Figure 3.

The steady-state dissolution rates for the group of 20 experiments are summarized in Figure 4 for the several pH values and ascorbic acid concentrations studied. The salient features are that the dissolution rate decreases with increasing pH and with decreasing ascorbic acid concentration. Simultaneously with the dissolution rate determinations, AFM micrographs are recorded every 4 min. Representative images prior to and during dissolution are shown in Figure 5. The image pairs {5*A*, 5*B*} and {5*C*, 5*D*} correspond respectively to the regions labeled 2 and 3 in Figure 4. For the points within region 2 of Figure 4, surface changes indicative of dissolution are apparent in {5*A*, 5*B*}. Processes include etching and step retreat. For the points within region 3, changes corresponding to surface precipitation are apparent in {5*C*, 5*D*}, though net dissolution is occurring as indicated by $[Mn^{2+}]_{effluent}$ assayed in the GF-AAS analysis.

Several additional interesting features are apparent in Figure 5. The solid white line reveals step retreat from image 5*A* to 5*B*. The pairs of arrows indicate in one case pit removal via apparent precipitation and in the second case apparent pit propagation to form a trench. Perusal of the image by the reader reveals several instances of trench formation. Moreover, these trenches appear to align in an organized framework, possibly in step with the underlying crystallography. The white oval highlights a region where surface retreat is apparent for several features.

In addition to the AFM micrographs shown in Figure 5, under many conditions the micrographs showed at most minor changes, and these micrographs are not shown. However, the results are summarized, as follows. Control experiments indicate no surface changes in the absence of ascorbic acid. In region 1, no surface changes are apparent, which is reasonably accounted for by the short duration of the AFM imaging (300 min) relative to the slow dissolution rates under these conditions (Figure 4). In control experiments in the absence of O_2, no surface precipitation is

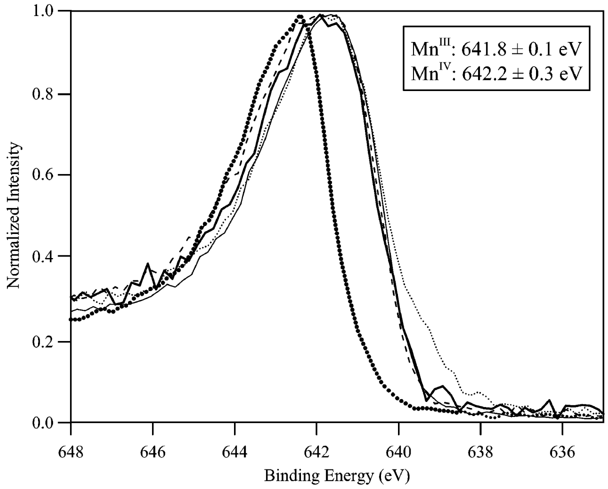

FIGURE 6. X-ray photoelectron spectra (XPS) of the Mn 2p$_{3/2}$ peak of manganite following exposure to 0.1 M ascorbic acid at pH = 5.9 for 1 h (···), 3 h (- - -), and 24 h (–). Reference spectra are also shown for manganite (—) and pyrolusite (•••).

observed for region 3, and the observed minor changes appear as step retreat.

To aid in the identification of the surface precipitate shown in Figure 5D, XPS spectra (Figure 6) are collected. Literature reports indicate the binding energy for Mn 2p$_{3/2}$ in the +III oxidation state occurs at 641.8 ± 0.1 eV, while in the +IV state the binding energy is 642.2 ± 0.3 eV (*31*, *43*). The measurements shown in Figure 6 are consistent with these values and show the Mn^{III} 2p$_{3/2}$ of γ-MnOOH at 641.8 ± 0.3 eV and the Mn^{IV} 2p$_{3/2}$ for β-MnO$_2$ at 642.4 ± 0.2 eV for the reference minerals employed. Following exposure to 0.1 M ascorbic acid at pH = 5.9, there is no evidence for the formation of a Mn^{IV} precipitate (i.e., absence of Mn$_3$O$_4$ and MnO$_2$). Similar results (not shown) are obtained at pH = 2.4 and 0.1 M ascorbic acid. Mn$_2$O$_3$ (bixbyite) as a possible precipitate is ruled out because a hydroxide peak is recorded at 530.4 eV in the O 1s spectrum (not shown) (*31*). We conclude that Mn^{III}OOH precipitates on surface. Although the collected XPS spectra do not distinguish between β-MnOOH (feitknechtite) and γ-MnOOH (manganite), a reasonable assumption is that a γ-MnOOH substrate will strongly favor a γ-MnOOH precipitate due to epitaxial interactions. There is no evidence in the literature for amorphous Mn^{III} hydroxide phases, in contrast to Fe(OH)$_3$ ferrihydrite accompanying Fe^{III} precipitation.

Discussion

The observations categorized as regions in Figure 4 reveal clear demarcations in the qualitative features of the dissolution processes. At low pH, etching and step retreat are apparent while precipitates form at higher pH values. The analysis below begins by presenting the thermodynamic driving forces behind a stepwise mechanism that succeeds in rationalizing the observations of the onset of precipitation. In subsequent sections, the implications of this mechanism on the apparent macroscopic dissolution rate are discussed, and comparisons with previous literature reports are provided.

Thermodynamic Driving Forces. The dissolution process is hypothesized by us to proceed in a first step by reductive dissolution of Mn^{III} by ascorbic acid to release aqueous Mn^{2+}. The rate-determining step is believed to be electron transfer in an inner sphere ascorbate–Mn^{III} surface complex (*11*). In a second step, the dissolved aqueous Mn^{2+} cations follow one of two pathways: a fraction diffuses to aqueous solution to be assayed by the GF-AAS while the remaining fraction adsorbs to the surface and subsequently oxidizes to form the MnOOH(s) observed in the AFM. This mechanism omits homogeneous oxidation of Mn^{2+} because the kinetics are slow for pH < 9 (*30*).

For pH > pK_{a1} of ascorbic acid, the half-reactions of step 1 of the hypothesized reaction pathway are as follows:

$$\mathrm{A^- \rightarrow 2\,H^+ + 2\,e^- + DHA^-} \qquad E^\circ_{1/2} = -0.40\ \mathrm{V} \quad (2)$$

$$\gamma\text{-}\mathrm{MnOOH + e^- + 3\,H^+ \rightarrow Mn^{2+} + 2\,H_2O} \qquad E^\circ_{1/2} = +1.50\ \mathrm{V} \quad (3)$$

$$2\,\gamma\text{-}\mathrm{MnOOH + A^- + 4\,H^+ \rightarrow 2\,Mn^{2+} + 4\,H_2O + DHA^-} \qquad E^\circ = +1.10\ \mathrm{V} \quad (4)$$

where A$^-$ is ascorbate and DHA$^-$ is dehydroascorbate (pK_a = 3.9) and the half-reaction potentials are referenced to NHE (*44*). We choose γ-MnOOH for our analysis; β-MnOOH is more endoergic by 3.5 kJ mol^{-1} (*45*). Following from eq 4 and omitting the effects of ionic strength and nonideal solutions, eq 5 provides the reaction driving force under conditions different from the standard state:

$$E_1 = +1.10 - 0.0296 \log \frac{[\mathrm{Mn^{2+}}]^2[\mathrm{DHA^-}]}{[\mathrm{H^+}]^4[\mathrm{A^-}]} \qquad (5)$$

Although the above calculations are for the circumneutral species A$^-$ and DHA$^-$ (which are dominant for pH > 5), for practical purposes eq 5 also holds for acidic pH because the standard reduction potential changes only slightly from +0.40 V for DHA$^-$/A$^-$ to +0.41 V for DHA/A, where A is ascorbic acid and DHA is dehydroascorbic acid.

Subsequent to Mn^{2+} release (eq 4), adsorption isotherms reported in the literature show that Mn^{2+}(aq) partitions between the aqueous boundary layer and a surface-adsorbed species (*26*, *31*). The surface-adsorbed species is susceptible to rapid oxidation by O$_2$(aq) (*18*). The oxidized species is insoluble and precipitates. The half-reactions describing step 2 of the hypothesized reaction pathway are as follows:

$$\mathrm{Mn^{2+} + 2\,H_2O \rightarrow \gamma\text{-}MnOOH + e^- + 3\,H^+} \qquad E^\circ_{1/2} = -1.50\ \mathrm{V} \quad (6)$$

$$\mathrm{O_2 + 4\,e^- + 4\,H^+ \rightarrow 2\,H_2O} \qquad E^\circ_{1/2} = +1.23\ \mathrm{V} \quad (7)$$

$$\mathrm{4\,Mn^{2+} + O_2 + 6\,H_2O \rightarrow 4\,\gamma\text{-}MnOOH + 8\,H^+} \qquad E^\circ = -0.27\ \mathrm{V} \quad (8)$$

Equation 9 provides the reaction driving force under conditions different from the standard state:

$$E_2 = -0.27 - 0.0148 \log \frac{[\mathrm{H^+}]^8}{[\mathrm{Mn^{2+}}]^4 P_{\mathrm{O_2}}} \qquad (9)$$

Contour plots of E_1 and E_2 are shown in Figure 7. The proposed pathway of dissolution (step 1, release of Mn^{2+}) followed by precipitation (step 2, readsorption of Mn^{2+} and oxidation) for region 3 points of Figure 4 is thermodynamically favorable only for those values of [Mn^{2+}] and pH for which $E_1 > 0$ and $E_2 > 0$. The triangles in Figure 7, which correspond to those data points indicating surface precipitation (region 3), indeed lie within the white region, which demarcates $E_1 > 0$ and $E_2 > 0$. Furthermore, the region 2 data points, for which surface precipitation is not observed in the AFM images, are shown as squares in Figure 7. These points lie in a region where dissolution is favorable ($E_1 > 0$) but precipitation is not ($E_2 < 0$). For region 1, dissolution is slow enough that surface changes are not observed in AFM imaging, at least for the time scale of our measurements. This thermodynamic analysis based upon a two-step reaction pathway thus successfully rationalizes the categorization of AFM images reported for Figure 4.

An alternative analysis to eq 9 is consideration of the saturation ratio. As shown in Figure 8, at circumneutral pH

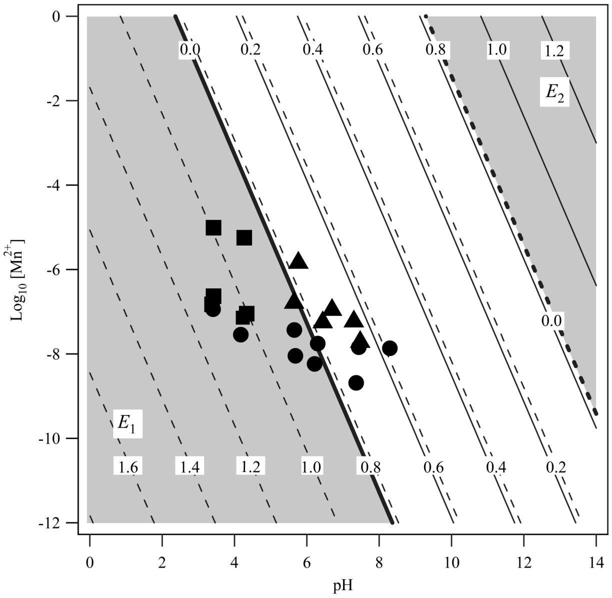

FIGURE 7. Contour plots of E_1 (V) for manganite reduction by ascorbic acid (step 1, eq 5) (dotted line) and of E_2 (V) for Mn^{2+} oxidation by O_2 to precipitate manganite (step 2, eq 9) (solid line). Gray regions indicate where either step 1 or 2 is not thermodynamically favorable. Key: Data points are from Figure 4, regions 1 (●), 2 (■), and 3 (▲). Conditions: $[A^-] = [DHA^-]$ in step 1 and $\log P_{O_2}$ (atm) $= -0.678$ in step 2.

the aqueous solution is metastable to several Mn^{III} and Mn^{IV} solids, though not to Mn^{II} solids. Under the reaction conditions of this work, the XPS analysis implicates the formation of a Mn^{III} solid. The data points in Figure 8 show that region 3 data points (Figure 4) are supersaturated with respect to manganite, so precipitation is thermodynamically favored. In contrast, region 2 data points lie in an undersaturated regime, so only surface dissolution is anticipated. Saturation ratios thus satisfactorily rationalize the onset of precipitation in the AFM observations.

The saturation ratio, *S*, of an aqueous solution with respect to manganite (Figure 8) is related to the potential (eq 9, Figure 7), as follows. First, by convention the solubility reaction is recognized as the reverse of eq 8 (i.e., the solid with unit activity is a reactant). Second, the fundamental relations for the solubility reaction are $\Delta G = -nF(-E_2) = -RT\ln(K/Q) = RT\ln S$. At 298 K it then follows:

$$E_2 = \frac{2.303R(298)}{4F}\log S = 0.0148\log S \qquad (10)$$

where $S = [Mn^{2+}]^4 P_{O_2}/10^{18.26}[H^+]^8$.

In this thermodynamic analysis, we assume that MnO_4^- and MnO_4^{2-} are not important products from reactions of Mn^{2+} under oxic conditions because the oxidation kinetics are slow. We omit MnO_4^- and MnO_4^{2-} in the thermodynamic treatment. However, if our assumption is not correct, the species become important for pH > 8.5.

Figures 7 and 8 show that the data are consistent with eqs 2–4 and 6–8 as the active chemical reactions. The data also exclude three other pathways. The disproportionation reaction is thermodynamically favorable:

$$\gamma\text{-MnOOH} + e^- + 3\,H^+ \rightarrow Mn^{2+} + 2\,H_2O \qquad E^\circ_{1/2} = +1.50\text{ V} \quad (11)$$

$$\gamma\text{-MnOOH} \rightarrow \beta\text{-MnO}_2 + e^- + H^+ \qquad E^\circ_{1/2} = +0.27\text{ V} \quad (12)$$

$$2\,\gamma\text{-MnOOH} + 2\,H^+ \rightarrow \beta\text{-MnO}_2 + Mn^{2+} + 2\,H_2O \qquad E^\circ = +1.77\text{ V} \quad (13)$$

Even so, both the dissolution data (Figure 4) and the AFM images show ascorbic acid is a necessary component in the reactions studied. In addition, the XPS data reveal no Mn^{IV} even after 24 h. Thus direct disproportionation can be ruled out, at least over the 300 min of these studies. Hem and Lind propose this reaction for aging for longer time periods (8 months) (*45*).

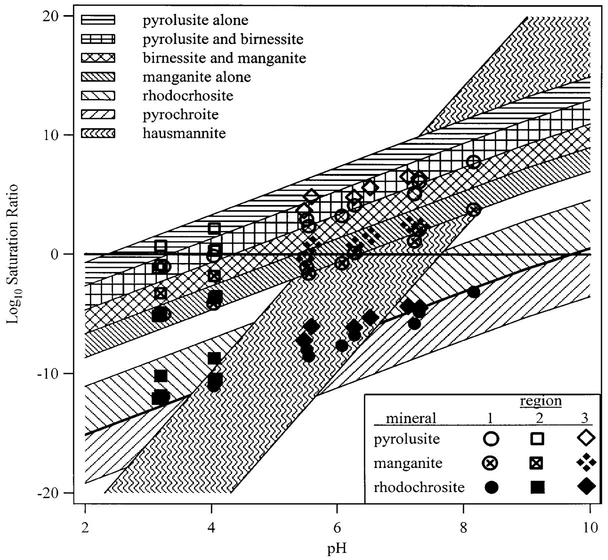

FIGURE 8. Plot of log saturation ratios (*S*) for several solids as a function of pH. System is open to the atmosphere ($\log P_{CO_2}$ (atm) $=$ -3.5 and $\log P_{O_2}$ (atm) $= -0.678$ [8.48 mg L^{-1}]) and solids precipitation is disallowed (i.e., calculations are for metastable aqueous solutions when $S > 1$). Hashed regions, which are coded in the figure legend, correspond to 10^{-8} (lower line) $< Mn_T < 10^{-4}$ M (upper line) for the solids pyrolusite, birnessite, manganite, hausmannite, rhodochrosite, and pyrochroite. Points are shown for saturation ratios with respect to pyrolusite, manganite, and rhodochrosite for the Mn_T concentrations corresponding to the dissolution rates data of Figure 4 (cf. eq 1). Saturation ratios are calculated in MINEQL+ ($Cl_T = 10^{-2}$ M and $NO_{3,T} = 10^{-2}$ M) using thermodynamic data therein and from Lindsay (*59*) for aqueous species (Mn^{2+}, Mn^{3+}, Mn^{4+}, $Mn(OH)^+$, $Mn(OH)_3^-$, $Mn(OH)_4^{2-}$, $H_2CO_3^*$, HCO_3^-, CO_3^{2-}, $MnHCO_3^+$, $MnCl^+$, $MnCl_3^-$, $MnCl_2^\circ$, $MnNO_3^+$, $Mn(NO_3)_2^\circ$, H^+, Cl^-, and NO_3^-). Note: Figures 7 and 8 are related by $E_2 = 0.01481\log S$ where $S = [Mn^{2+}]^4 P_{O_2}/10^{18.26}[H^+]^8$.

Although direct oxidation is also thermodynamically favorable (eq 16), it appears not to occur, as implicated by the absence of Mn^{IV} in the XPS data as well as the absence of changes in the AFM images when ascorbic acid is excluded from the system.

$$\gamma\text{-MnOOH} \rightarrow \beta\text{-MnO}_2 + e^- + H^+ \qquad E^\circ_{1/2} = +0.27\text{ V} \quad (14)$$

$$O_2 + 4\,e^- + 4\,H^+ \rightarrow 2\,H_2O \qquad E^\circ_{1/2} = +1.23\text{ V} \quad (15)$$

$$4\,\gamma\text{-MnOOH} + O_2 \rightarrow 4\,\beta\text{-MnO}_2 + 2\,H_2O \qquad E^\circ = +1.50\text{ V} \quad (16)$$

The absence of dissolution is not evidence in itself against eq 16 because no Mn^{2+} is released.

A nonreductive dissolution pathway, which is probably significant under highly acidic conditions, is also thermodynamically favorable:

$$\gamma\text{-MnOOH} + 3\,H^+ \rightarrow Mn^{3+} + 2\,H_2O\text{ (slow)} \qquad E^\circ_{1/2} = +1.50\text{ V} \quad (17)$$

$$2\,H_2O + 2\,Mn^{3+} \rightarrow Mn^{2+} + \beta\text{-MnO}_2 + 4\,H^+\text{ (fast)} \qquad E^\circ_{1/2} = +0.27\text{ V} \quad (18)$$

$$2\,\gamma\text{-MnOOH} + 2\,H^+ \rightarrow \beta\text{-MnO}_2 + Mn^{2+} + 2\,H_2O \qquad E = +1.77\text{ V} \quad (19)$$

The overall stoichiometric reaction is identical to eq 13 above. The same line of reasoning then rules out this reaction as a significant contributor in our studies.

Apparent Dissolution Rate. The apparent macroscopic dissolution rate (R_{app}) is the intrinsic reductive dissolution rate (R_{int}) minus the oxidative precipitation rate (R_{prec}). In the absence of precipitation (i.e., region 2 of Figure 4), the apparent and intrinsic dissolution rates are equal. For these cases, mechanistic implications may be drawn between the intrinsic dissolution rate and the concentrations of surface species (e.g., inner-sphere ligand surface groups) as commonly reported in the literature (*10*, *11*, *46*, *47*). When precipitation occurs (i.e., region 3 of Figure 4), the apparent dissolution rate is a lower limit of the intrinsic dissolution rate. In this case, attempts to correlate rates with surface species concentrations should not be successful and, in cases when they are, should be understood as coincidental, from which any mechanistic inference would be in error. In the absence of a surface sensitive technique to indicate when precipitation occurs, interpretation of apparent dissolution rates is problematic.

We can estimate an approximate precipitation rate from the vertical growth rates (dz/dt) for the region 3 data sets. Assuming precipitation is evenly distributed across the surface, as in accord with features in Figure 5, panels C and D, the oxidative precipitation rate is estimated as follows:

$$R_{prec} = (dz/dt)V_m \tag{20}$$

for a molar volume (V_m) of 4.9×10^4 mol m^{-3} (*48*). The dz/dt values are determined from cross-section analysis of a time series of AFM height images (not shown) for region 3 data points. For example, at pH = 5.5 and 10^{-3} M ascorbate, eq 20 yields a precipitation rate (R_{prec}) of 1.2×10^{-7} mol m^{-2} s^{-1}, while analysis of the effluent via eq 1 yields the apparent dissolution rate (R_{app}) of 3.7×10^{-7} mol m^{-2} s^{-1}. Summing these values yields the intrinsic dissolution rate (R_{int}) of 4.9×10^{-7} mol m^{-2} s^{-1}, corresponding to (R_{prec}/R_{int}) of 24%. At a higher pH, (R_{prec}/R_{int}) values are expected to be larger because the driving force for step 2 increases. Indeed, at pH = 7.2 and 10^{-2} M ascorbate, (R_{prec}/R_{int}) is 71%.

Growth in the vertical must be explained because overall the surface is dissolving and retreating, as implied by the high concentrations of [Mn^{2+}] in the cell effluent. There are two possibilities apparent to us, both of which serve to highlight the sometimes myopic observations of the AFM technique. One, dissolution may occur differentially across the surface whereas the AFM observations are localized. Two, the absolute height of the average plane of an image, as opposed to relative heights of pixels within an image, is not measured. It is then possible the average plane is retreating, while the roughness of the surface, which contributes to the apparent growth in z, is increasing. The assumption in this analysis is that the density of the precipitate is the same as the underlying substrate, and a third alternative is thus that the precipitate is porous and is thus able to increase volume (z height) with fewer Mn atoms.

An important check on the accuracy of our interpretation of the kinetic observations is to verify that the rate-limiting step is Mn-oxide precipitation, as opposed to other processes in the coupled mechanism, such as the rate of oxygen diffusion to the surface. To estimate the limiting rate for mass transfer flux of O_2, we employ Fick's law integrated for a flat boundary layer (*49*), as follows:

$$J_{O_2} = D(C_{surf} - C_{bulk})/L \tag{21}$$

Assuming a boundary layer thickness (L) of 100 nm and an aqueous diffusion coefficient (D) of 10^{-5} cm^2 s^{-1}, we then obtain a maximum oxygen flux (J_{O_2}) of 2.7×10^{-3} mol m^{-2} s^{-1}, which is much greater than the estimated precipitation rates. O_2 can then be assumed to be thoroughly mixed in our system along the height axis.

We must also verify that the perturbation on the total O_2 reservoir is small. Employing a reactor residence time of 20 s with a plugflow approximation and a maximum observed precipitation reaction rate of 10^{-6} mol m^{-2} s^{-1}, we obtain 2×10^{-5} mol m^{-2} as the upper limit of O_2 reacted. In comparison, the lower limit of the O_2 reservoir is 1.7×10^{-2} mol m^{-2}, which follows by calculation based upon 2.7×10^{-4} M O_2 (0.21 atm), a reactor height of 7.1×10^{-3} m, and a sample-to-reactor surface area ratio of 0.11. Because the lower limit of the reservoir exceeds the upper limit of O_2 reacted, we conclude that there is no gradient in O_2 along the length axis of the reactor.

Comparison with Previous Work. In contrast to literature reports by Junta and Hochella (*31*, *50*) on the heterogeneous oxidation of aqueous Mn^{2+} at hematite, goethite, and albite surfaces, our current work shows that the oxidation of aqueous Mn^{2+} on manganite does not show any specific preference for steps and kinks, at least for the conditions of our study. Precipitation at specific surface decorations such as steps is favored when surface diffusion rates are more rapid than precipitation rates: the surface is able to reorganize to minimize surface area and total surface energy. A general statement is that slow precipitation rates occur with low saturation ratios, though the specific rates of surface diffusion and precipitation and hence their ratio are highly dependent on a number of factors, including temperature, saturation ratio, surface presentation, and myriad chemical factors (*51*, *52*). Low saturation ratios favor the observations of Junta and Hochella in which precipitates show specific preference for steps. A further general statement is that at high saturation ratios and hence rapid precipitation rates, a film of hillocks is favored because precipitate growth is much more rapid than the characteristic times of surface reorganizations. These general principles provide the context for analyzing the differences between our observations and those of Junta and Hochella. Foremost, their precipitation rates of MnOOH can be estimated as 10^{-7} mol m^{-2} s^{-1} at pH = 8.15 as compared to 10^{-6} mol m^{-2} s^{-1} at pH = 7 in our work.

Junta and Hochella conducted their AFM work at 298 K over a narrow pH range ($7.8 < pH < 8.7$) under oxic conditions. In comparison to our work, in addition to pH several other experimental differences can be recognized. (1) The experimental time period ranged from a few minutes to 6 months, which is much longer than our experimental time period (usually 300 min). Surface reorganization favoring the features observed by Junta and Hochella could occur over a longer time period. (2) Manganite as a substrate for $>Mn^{2+}$ oxidation has four times more surface sites per unit area than iron oxides (4.37×10^{15} sites cm^{-2} for manganite and 1.0×10^{15} for hematite) (*53*, *54*). If all sites are presumed of equal reactivity, the oxidation rate should be faster for manganite. Our analysis discussed below for studies by Davies and Morgan (*26*) in fact suggests Mn-oxides may be 10^8 times more reactive than Fe-oxides. Rapid precipitation favors the film formation we observe.

Weaver reports on the reductive dissolution of manganite by Cr^{3+} (aq) and the consequent oxidation of Cr^{3+} (e.g., $CrOH^{2+}$ (aq) to Cr^{6+} (e.g., $HCrO_4^-$, chromate)) at 298 K over a pH range of 3−6 (*55*). AFM observations show etching and step retreat are heterogeneous across the manganite surface, and no general rule is apparent concerning sites more favorable toward dissolution. These observations are consistent with ours in Figure 5, panels A and B. Simultaneous with dissolution, at higher pH values, portions of the manganite surface show a precipitate identified as $Cr(OH)_3 \cdot 3H_2O$. The precipitates are distributed without any discernible preference for specific surface sites, such as steps and kinks. At pH = 6 and a similar ionic strength and time period, the reductive dissolution rate by Cr^{3+} is 5.3×10^{-8} mol m^{-2} s^{-1} as compared to the reductive dissolution rate by ascorbate of 5.5×10^{-7} mol m^{-2} s^{-1} in our work. The slower dissolution rate offers an explanation for the absence of Mn−(hydr)-oxide precipitates in Weaver's experiments, though possible inhibition effects by Cr^{3+} are not ruled out.

Stumm et al. (*56*) and Davies and Morgan (*26*) discuss surface-catalyzed oxidation of aqueous Mn^{2+} by O_2 on metal oxides. Mn^{2+} ions are believed to specifically adsorb to a manganese oxide surface via linkage to a lattice oxygen. This inner-sphere complex promotes oxidation because the hydroxo-coordination facilitates the outer- or inner-sphere attachment of O_2 molecules. Employing these literature reports (viz. eq 30 of ref *26* as eq 22a), we can estimate the rate of Mn^{2+} oxidative precipitation on the manganite, as follows:

$$R_1\ (\mathrm{M\ s^{-1}}) = k_{(\mathrm{atm^{-1}\,s^{-1}})}\{>S\}_{(\mathrm{mol/g})}\frac{A_{(\mathrm{g})}}{V_{(\mathrm{L})}}P_{\mathrm{O_2(atm)}} \tag{22a}$$

$$= R_2\ (\mathrm{mol\ m^{-2}\ s^{-1}})\frac{A_{(\mathrm{m^2})}}{V_{(\mathrm{L})}} \tag{22b}$$

where R_1 and R_2 are the volume-normalized and surface-normalized precipitation rates, respectively, k is the rate coefficient (atm^{-1} s^{-1}), $\{>S\}$ is the concentration of manganese on the mineral surface (mol g^{-1}), $A_{(g)}$ is the particulate mass (g), $A_{(m^2)}$ is the particulate surface area (m^2), P_{O_2} is partial pressure of O_2 (atm), and V is the container volume of the aqueous particulate suspension (L). Equation 22b is derived by considering the release rate of metal ion to solution in a particulate suspension of particle loading $A_{(m^2)}/V_{(L)}$ dissolving at rate R_2. Recognizing $A_{(m^2)}/A_{(g)}$ as BET surface area, we develop eq 22b as follows:

$$R_2 = k\{>S\}(\mathrm{BET}_{\mathrm{m^2/g}})^{-1}P_{\mathrm{O_2}} \tag{23a}$$

$$= \frac{kP_{\mathrm{O_2}}}{\mathrm{BET}_{(\mathrm{m^2/g})}}\left[\beta_2\frac{[\mathrm{Mn}^{2+}]\{>\mathrm{SOH}\}_{(\mathrm{mol/g})}}{[\mathrm{H}^+]^2}\right] \tag{23b}$$

$$= k\beta_2P_{\mathrm{O_2}}\left[\frac{[\mathrm{Mn}^{2+}][>\mathrm{SOH}]_{(\mathrm{mol/m^2})}}{[\mathrm{H}^+]^2}\right] \tag{23c}$$

We use eq 9 of ref *26* to replace $\{>S\}$. Because we assume that most of Mn(II) surface complexes are bidentate, β_2 is the intrinsic binding constant (M) of the bidentate complex. $\{>\mathrm{SOH}\}$ is the site density of OH groups (mol/g). Numerical values are as follows: $k = 8.7 \times 10^{-4}$ atm^{-1} s^{-1}, $\beta_2 = 10^{-12.7}$ M, and $[>\mathrm{SOH}] = 1.6 \times 10^{-5}$ mol m^{-2} (Tables I, III, and VIII of ref *26*). The numerical values quoted are for γ-FeOOH because values for γ-MnOOH are not available (*26*). At pH = 7 and $[Mn^{2+}] = 10^{-7}$ M, R_2 is 6×10^{-14} mol m^{-2} s^{-1} when calculated from eq 23c by employing parameter values of γ-FeOOH. This value for R_2 does not agree with our measured R_{prec} of 10^{-6} mol m^{-2} s^{-1} at pH = 7. To account for the large difference between calculated and measured values, $k\beta_2$ of γ-MnOOH must exceed $k\beta_2$ of γ-FeOOH by a factor of 10^8.

Another critical value in eq 23c is $[Mn^{2+}]$. Previous studies of surface catalyzed Mn^{2+} oxidation (eq 8) spiked aqueous Mn^{2+} in the reactor (*18, 26, 57*). There is thus concern that near surface concentrations are less than the bulk medium if oxidation is more rapid than mass transfer. Davies and Morgan, however, argued that a rapid adsorption isotherm is maintained (*26*). Our study is fundamentally different from the previous work, however, in the sense that Mn^{2+} has an in situ surface source. Near surface concentrations may thus be supposed to be greater than those in the bulk. Hem has previously raised this concern in his thermodynamic analysis of transformations of lower oxides of manganese during aging with O_2 to higher oxidation state oxides, in which a two-step pathway involving Mn^{2+} oxidation at the surface is postulated (*45, 58*). Employing eq 21 adapted for Mn^{2+}, we can estimate the difference between surface and bulk concentrations. Assuming the intrinsic dissolution rate equals the apparent rate so as to obtain upper limits of the difference values, the maximum percentage difference (57%) occurs for pH = 7.3 and $[\mathrm{Mn}^{2+}]_{\mathrm{bulk}} = 2.2 \times 10^{-8}$ M ($J = 1.3 \times 10^{-7}$ mol m^{-2} s^{-1}, $D = 10^{-5}$ cm^{-2} s^{-1}, $L = 100$ nm, and then solve eq 21 for C_{surf}.) We thus conclude that, within uncertainties in our overall analysis, the surface concentrations of $[Mn^{2+}]$ may be taken as the bulk concentrations assayed by the GF-AAS analysis. In this case, employing the adsorption isotherm inherent in the rate equation of Davies and Morgan seems reasonable.

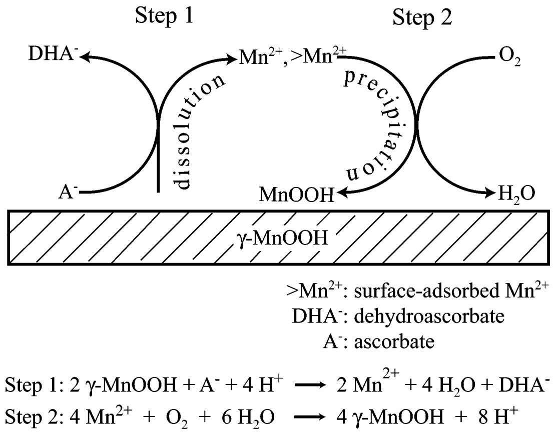

FIGURE 9. Chemical cycles of surface dissolution and precipitation.

The major mechanistic insights of the current work are depicted by the schematic diagram shown in Figure 9. In step 1 (eqs 2−5), Mn^{2+} is released to aqueous solution by ascorbic acid reduction. This step is thermodynamically favorable under all conditions employed in the current study and appears as etching and step retreat in the AFM micrographs. In step 2 (eqs 6−9), surface-adsorbed Mn^{2+} is oxidized by O_2 to yield a Mn^{III}-oxide precipitate. This step is favorable only at pH > 5 for the conditions of this study and appears as a precipitate in the AFM micrographs. When the second step is active, the apparent dissolution rate equals the intrinsic dissolution rate minus the precipitation rate. Analysis of the growth rates observed in AFM indicates the precipitation rate reaches 71% of the intrinsic rate under some reactor conditions (viz. higher pH values). This result emphasizes the need for microscopic studies to understand mechanisms of mineral dissolution. When precipitation occurs, macroscopic studies that attempt to offer mechanistic insight, which is often done under the unstated assumption that the apparent dissolution rate is the intrinsic dissolution rate, will be flawed. The current study also emphasizes the dynamic and complex nature of oxic/anoxic transition zones of soils, in the rhizosphere, and in biofilms, in which several opposing processes such as dissolution and precipitation occur concurrently. Although the net process may be either dissolution or precipitation, accurately modeling the time-dependent morphological development of solids requires including both pathways, as does any accurate and mechanistic description of the net process.

Acknowledgments

We are grateful for support received from the New York Community Trust Merck Fund, the Petroleum Research Fund, Materials Research Science and Engineering Center, and the Harvard Mineralogical Museum. We thank Cynthia Friend, Ally Chan, Alan Stone, and Owen Duckworth for valuable discussion.

Literature Cited

(1) Klinchuch, L. A.; Delfino, T. A. *Environ. Geosci.* **2000**, *7*, 69.

(2) Hudson-Edwards, K. A. In *Environmental Mineralogy: Microbial Interactions, Anthropogenic Influences, Contaminated Land and Waste Management*; Cotter-Howells, J. D., Campbell, L. S., Valsami-Jones, E., Batchelder, M., Eds.; The Mineralogical Society of Great Britain and Ireland, 2000; Vol. 9.

(3) Davies, S. H. R. In *Geochemical Processes at Mineral Surfaces*; Davies, J. A., Hayes, K. F., Eds.; American Chemical Society: Washington, DC, 1986.

(4) Hem, J. D. *Geol. Soc. Am. Bull.* **1972**, *83*, 443.

(5) Jeffrey, D. W. In *Soil Solution Chemistry*; Wiley: New York, 1994.

(6) Stumm, W.; Morgan, J. J. *Aquatic Chemistry*, 3rd ed.; Wiley: New York, 1996.

(7) Richardson, L. L.; Aguilar, C.; Nealson, K. H. *Limnol. Oceanogr.* **1988**, *33*, 352.

(8) Sunda, W. G.; Huntsman, S. A. *Limnol. Oceanogr.* **1987**, *32*, 552.

(9) Silver, M.; Ehrlich, H. L.; Ivarson, K. C. In *Interactions of Soil Minerals with Natural Organics and Microbes*; Huang, P. M., Schnitzer, M., Eds.; SSSA: Wisconsin, 1986; Vol. 17.

(10) Stone, A. T.; Morgan, J. J. *Environ. Sci. Technol.* **1984**, *18*, 617.

(11) Stone, A. T. *Environ. Sci. Technol.* **1987**, *21*, 979.

(12) Stone, A. T.; Morgan, J. J. In *Aquatic Surface Chemistry: Chemical Processes at the Particle−Water Interface*; Stumm, W., Ed.; Wiley: New York, 1987.

(13) Marschner, H. *Mineral Nutrition of Higher Plants*; Academic Press: San Diego, 1995.

(14) Jones, D. *Plant. Soil.* **1998**, *205*, 25.

(15) Lopez-Bucio, J.; Nieto-Jacobo, M. F.; Ramirez-Rodriguez, V.; Herrera-Estrellav, L. *Plant Sci.* **2000**, *160*, 1.

(16) Curl, E. A.; Truelove, B. *The Rhizosphere*; Springer-Verlag: New York, 1986.

(17) Little, B. J.; Wagner, P. A.; Lewandowski, Z. In *Geomicrobiology: Interactions between Microbes and Minerals*; Banfield, J. F., Nealson, K. H., Eds.; Mineralogical Society of America: Washington, DC, 1997; Vol. 35.

(18) Wehrli, B. In *Aquatic Chemical Kinetics*; Stumm, W., Ed.; Wiley: New York, 1990.

(19) Hem, J. D. *Chem. Geol.* **1978**, *21*, 199.

(20) Stone, A. T.; Morgan, J. J. *Environ. Sci. Technol.* **1984**, *18*, 450.

(21) Stone, A. T. *Geochim. Cosmochim. Acta* **1987**, *51*, 919.

(22) Xyla, A. G.; Barbara, S.; Luther, I., George W.; G., H. J.; Van, C. P.; Stumm, W. *Langmuir* **1992**, *8*, 95.

(23) Klewicki, J. K.; Morgan, J. J. *Geochim. Cosmochim. Acta* **1999**, *63*, 3017.

(24) Banerjee, D.; Nesbitt, H. W. *Geochim. Cosmochim. Acta* **2001**, *65*, 1703.

(25) Banerjee, D.; Nesbitt, H. W. *Geochim. Cosmochim. Acta* **1999**, *63*, 3025.

(26) Davies, S. H. R.; Morgan, J. J. *J. Colloid Interface Sci.* **1989**, *129*, 63.

(27) Wehrli, B.; Friedl, G.; Alain, M. In *Aquatic Chemistry: Interfacial and Interspecies Processes*; Huang, C. P., O'Melia, C. R., Morgan, J. J., Eds.; American Chemical Society: Washington, DC, 1995; Vol. 244.

(28) Diem, D.; Stumm, W. *Geochim. Cosmochim. Acta* **1984**, *48*, 1571.

(29) Hem, J. D. *Geochim. Cosmochim. Acta* **1981**, *45*, 1369.

(30) Sung, W.; Morgan, J. J. *Geochim. Cosmochim. Acta* **1981**, *45*, 2377.

(31) Junta, J. L.; Hochella, M. F., Jr. *Geochim. Cosmochim. Acta* **1994**, *58*, 4985.

(32) Budavari, S.; O'Neil, M. J.; Smith, A.; Heckelman, P. E.; Kinneary, J. F. *The Merck Index*, 12th ed.; 1996.

(33) Stone, A. T.; Godteredsen, K. L.; Deng, B. In *Chemistry of Aquatic Systems: Local and Global Perspectives*; Bidoglio, G., Stumm, W., Eds.; 1994.

(34) Xu, J.; Jordan, R. B. *Inorg. Chem.* **1990**, *29*, 4180.

(35) Afonso, M. D. S.; Morando, P. J.; Blesa, M. A.; Banwart, S. A.; Stumm, W. *J. Colloid Interface Sci.* **1990**, *138*, 74.

(36) Banwart, S. A.; Davies, S.; Stumm, W. *Colloid. Surface* **1989**, *39*, 303.

(37) Duckworth, O. W.; Martin, S. T. *Geochim. Cosmochim. Acta* **2003**, *67*, 1787.

(38) Murray, J. W.; Dillard, J. G.; Giovanoli, R. *Geochim. Cosmochim. Acta* **1985**, *49*, 463.

(39) Hochella Jr., M. F. In *Spectroscopic Methods in Mineralogy and Geology*; Hawthorne, F. C., Ed.; Mineralogical Society of America: Washington, DC, 1988; Vol. 18.

(40) Shiraki, R.; Rock, R. A.; Casey, W. H. *Aquat. Geochem.* **2000**, *6*, 87.

(41) Samson, S. D.; Eggleston, C. M. *Environ. Sci. Technol.* **1998**, *32*, 2871.

(42) Samson, S. D.; Eggleston, C. M. *Geochim. Cosmochim. Acta* **2000**, *64*, 3675.

(43) Nesbitt, H. W.; Banerjee, D. *Am. Mineral.* **1998**, *83*, 305.

(44) Bard, A. J.; Faulkner, L. R. *Electrochemical Methods*; Wiley: New York, 1980.

(45) Hem, J. D.; Lind, C. J. *Geochim. Cosmochim. Acta* **1983**, *47*, 2037.

(46) Furrer, G.; Stumm, W. *Geochim. Cosmochim. Acta* **1986**, *50*, 1847.

(47) Ulrich, H.-J.; Stone, A. T. *Environ. Sci. Technol.* **1989**, *23*, 421.

(48) Klein, C.; Hurlbut, J. C. S. *Manual of Mineralogy*, 21st ed.; Wiley: New York, 1999.

(49) Schwarzenbach, R. P.; Gschwend, P. M.; Imbolden, D. M. *Environmental Organic Chemistry*; Wiley: New York, 1993.

(50) Junta-Rosso, J. L.; Hochella Jr., M. F.; Rimstidt, J. D. *Geochim. Cosmochim. Acta* **1997**, *61*, 149.

(51) Corey, R. B. In *Adsorption of Inorganics at Solid−Liquid Interfaces*; Anderson, M. A., Rubin, A. J., Eds.; Ann Arbor Science Publishers: Ann Arbor, 1981.

(52) Morel, F. M. M.; Hering, J. G. In *Principles and Applications of Aquatic Chemistry*; Wiley: New York, 1993.

(53) Matsui, I. Ph.D. Dissertation, Lehigh University, 1973.

(54) Coughlin, R. W.; Matsui, I. *J. Catal.* **1976**, *41*, 108.

(55) Weaver, R. M. Ph.D. Dissertation, Virginia Polytech Institute and State University, 2001.

(56) Stumm, W.; Barbara, S.; Jürich, S. *Croat. Chem. Acta* **1990**, *63*, 277.

(57) Wehrli, B.; Sulzberger, B.; Stumm, W. *Chem. Geol.* **1989**, *78*, 167.

(58) Hem, J. D.; Roberson, C. E.; Fournier, R. B. *Water Resour. Res.* **1982**, *18*, 563.

(59) Lindsay, W. L. In *Chemical Equilibria in Soils;* Wiley: New York, 1979.

Received for review October 22, 2002. Revised manuscript received February 19, 2003. Accepted March 1, 2003.

ES026254X